



**HAL**  
open science

## Microstructure reconstruction of fibrous C/C composites from X-ray microtomography

Julio Martin-Herrero, Christian Germain

► **To cite this version:**

Julio Martin-Herrero, Christian Germain. Microstructure reconstruction of fibrous C/C composites from X-ray microtomography. *Carbon*, 2007, 45 (5), pp.1242-1253. 10.1016/j.carbon.2007.01.021 . hal-00166485

**HAL Id: hal-00166485**

**<https://hal.science/hal-00166485>**

Submitted on 6 Aug 2007

**HAL** is a multi-disciplinary open access archive for the deposit and dissemination of scientific research documents, whether they are published or not. The documents may come from teaching and research institutions in France or abroad, or from public or private research centers.

L'archive ouverte pluridisciplinaire **HAL**, est destinée au dépôt et à la diffusion de documents scientifiques de niveau recherche, publiés ou non, émanant des établissements d'enseignement et de recherche français ou étrangers, des laboratoires publics ou privés.

# 1 Microstructure reconstruction of fibrous C/C 2 composites from X-ray microtomography

3 J. Martín-Herrero <sup>a,\*</sup>, Ch. Germain <sup>b</sup>

4 <sup>a</sup>*Dept. Signal Theory and Communications, Univ. of Vigo, 36310-Vigo SPAIN*

5 <sup>b</sup>*Equipe Signal et Image, LAPS-UMR 5131 CNRS, Univ. Bordeaux1,  
6 33405-Talence FRANCE*

---

## 7 Abstract

8 The precise characterization of the microstructure of fibrous composites is essential  
9 for an accurate determination of their properties and behaviour. However, fabrica-  
10 tion processes usually introduce serious deviations from simple ideal spatial arrange-  
11 ments of preform fibres and matrix. The characterization of composites has been  
12 performed using destructive and non destructive testing techniques, many of them  
13 based on image analysis. Carbon fibres in carbon matrix composites, however, pose  
14 a difficult challenge to image analysis systems due to the poor contrast between  
15 the different phases. We describe a procedure for the reconstruction of the true  
16 microstructure of carbon/carbon composites using phase contrast X-ray microto-  
17 mography, show some results, and discuss its performance.

18 *Key words:* Carbon/carbon composites, Chemical vapor infiltration, Image  
19 analysis, Microstructure

---

\* Corresponding author. FAX: +34 986 812 116  
*Email address:* julio@uvigo.es (J. Martín-Herrero).

## 20 **1 Introduction**

21 The special properties of fibre reinforced composites responsible for their suc-  
22 cess are based on their inherent anisotropy, a characteristic dictated by the spa-  
23 tial arrangement of the constituent phases. Indeed, the microscopic arrange-  
24 ment of the complex fibrous structure and matrix plays a major role in the  
25 determination of the macroscopic properties of the material, such as their elas-  
26 ticity, strength, permeability, or thermal conductivity. As such, there is a whole  
27 range of numerical methods designed to estimate bulk properties assuming the  
28 characteristics of the phases and their spatial arrangement are known, such as  
29 those based on Finite Elements Models. Among the structural characteristics  
30 that influence the properties of the material are those regarding the fibres,  
31 such as the distribution of lengths and orientations, waviness, curvature, and  
32 volume fraction, and similar quantities for the matrix and void phases. Man-  
33 ufacturing techniques are fine tuned to control these characteristics, but the  
34 tuning process usually requires repeated cycles of fabrication and comparison  
35 with characterized samples. The recent advances in computer aided modelling  
36 and simulation have not eliminated the necessity of experimental work, but  
37 rather have increased the demand of accurate experimental data for training,  
38 testing, and validation, once the early models based on ideal, regular, or uni-  
39 form structures have been superseded. Moreover, no matter how much fine  
40 tuning, there is no such a thing as the perfect manufacturing process and,  
41 therefore, different factors in the fabrication chain introduce in the real mi-  
42 crostructure of the product deviations from the theoretical design which affect  
43 the predicted performance of the material.

44 Costly, limited, error-prone manual methods [1, 2] for the characterization

45 of samples of fibrous composites have been outdated by automatic methods,  
46 such as those in [3–20], using modern imaging systems [21] and digital image  
47 processing [22]. Most of them are based on optical microscopy, and therefore  
48 limited to the study of a 2D cross-section, serial sectioning, or, at most, limited-  
49 depth volumes of translucent materials using optical confocal microscopy [23].  
50 However, only some aspects of the 3D microstructure can be reconstructed  
51 from a 2D section, such as fiber orientation [20], subject to a series of assump-  
52 tions [24]. Producing and analyzing series of close, thin parallel slices of the  
53 samples [25], such as in [7, 9, 11, 19], is labour intensive and adds the problem  
54 of matching among slices.

55 X-ray microtomography [26, 27] is a non destructive technique that produces  
56 accurate images of 3D volumes by reconstruction from multiple X-ray pro-  
57 jections [28], allowing the direct characterization of the 3D microstructure of  
58 samples with significant thickness. The huge amount of data produced by this  
59 kind of imaging system for large enough samples, even at moderate resolu-  
60 tions, precludes any manual processing such as fibre identification. However,  
61 2D image processing techniques usually do not have a direct translation into  
62 the 3D domain, and processing a 3D microtomograph just as a series of 2D  
63 sections is clearly a waste of valuable information. Therefore, specific 3D tech-  
64 niques are needed [29, 30], but the combined effect of the increased amount of  
65 data to process and the added dimension (most processing algorithms scale  
66 geometrically with the dimension of the dataset) calls for extreme care in the  
67 selection of the methods and their optimization.

68 Carbon/carbon (C/C) fibre reinforced composites [31] are made of carbon fi-  
69 bres embedded in a continuous matrix of carbon. The fact of both matrix  
70 and fibres being fabricated from carbon produces a unique combination of

71 properties, including very low thermal expansion coefficients and high ther-  
72 mal conductivity, retaining their mechanical properties at high temperatures  
73 ( $> 2000^{\circ}\text{C}$  in nonoxidizing atmospheres), high specific strength, excellent re-  
74 sistance to abrasion and ablation, high resistance to thermal shock, very high  
75 elastic modulus, low density, high electrical conductivity, low hygroscopicity,  
76 nonbrittle failure, low biological rejection, resistance to chemical corrosion,  
77 and reasonable machinability [32].

78 However, C/C composites pose a significant challenge to X-ray imaging sys-  
79 tems due to the close densities of inclusions and matrix, yielding very poor  
80 contrast among the constituent phases. Sensitivity can be increased for com-  
81 posites made up of materials with neighbouring densities such as C/C compos-  
82 ites by using coherent X-rays (e.g. from a synchrotron source) and varying the  
83 distance from sample to detector [27]. Yet this technique, called holotomogra-  
84 phy, applies only to very small C/C samples for which all fibres show the same  
85 orientation. Indeed, in larger samples, or in samples where fibres perpendic-  
86 ular to the tomography occur, these fibres cause very high cumulated phase  
87 lag values which saturate the detector. The resulting image is blurred, render-  
88 ing the separation of fibres and matrix impossible [33]. The alternative, also  
89 requiring a coherent X-ray source, is phase contrast tomography, also called  
90 edge-detection mode CMT, where interfaces between constituent phases are  
91 detected through the interference patterns arising from the out of phase waves  
92 propagated through materials with different refraction indices [34].

93 Previous attempts have been made to characterise the microstructure of a  
94 C/C composite using X-ray microtomography [18, 34]. However, the carbon  
95 matrix proved to be very difficult to separate from the carbon fibres, and only  
96 the separation of the porosity from the solid phases was achieved. Later, the

97 method was successfully applied to the separation of the three phases in an  
98 Al-SiC<sub>p</sub> composite [35, 36]. On the other hand, the X-ray microtomography  
99 segmentation procedures in [29, 30] deal with easily separable phases, such as  
100 glass fibres in a polypropylene matrix, therefore the constituents are clearly  
101 resolved in the microtomographs and the segmentation phase is straightfor-  
102 wardly addressed by simple thresholding, ineffective in the case of a C/C  
103 composite synchrotron X-ray microtomography.

104 In the following, we will show a procedure for the reconstruction of the 3D  
105 microstructure of a C/C fibrous composite from a phase contrast X-ray mi-  
106 crotomography, based on advanced image processing techniques, allowing the  
107 separation of fibres, porosity, and matrix, and the subsequent analysis, char-  
108 acterization, and even visualization by means of enhanced reality techniques  
109 as an aid to design and analysis. Section 2 describes a sample we use as study  
110 case to illustrate the method, described in section 3. The description is ac-  
111 companied by some results obtained with the study sample. Finally, section 4  
112 is a brief discussion and section 5 closes with a short summary.

## 113 **2 A C/C fibre reinforced composite microtomographic image**

114 The image in Figure 1 was obtained at the European Synchrotron Radia-  
115 tion Facility (ESRF) ID19 High Resolution Diffraction Topography Beamline,  
116 dedicated to radiography, microtomography, and diffraction imaging experi-  
117 ments [27, 34]. The X-ray beams produced at third generation synchrotron  
118 radiation facilities such as the ESRF at Grenoble (France) have a high de-  
119 gree of coherence. This results from the small source size,  $\sigma$ , about 50  $\mu\text{m}$ ,  
120 and the large distance from source to sample,  $L$ , in the 100 m range, so that

121 the transverse coherence length,  $dc = \lambda L/2\sigma$ , is in the 100  $\mu\text{m}$  range. Phase  
122 changes occur at the edges of a particle or porosity embedded in a matrix  
123 having a different index of refraction, and out of phase transmitted radiations  
124 produce an interference fringe marking the location of the interface. The im-  
125 age shown was obtained using phase contrast with fixed distance from sample  
126 to detector [34].

127 The sample comes from the French aeronautics industrial company Snecma  
128 Propulsion Solide (SPS). SPS has decades of experience in isothermal chemical  
129 vapour infiltration (CVI) [32,37,38] for the development of proprietary C/C,  
130 C/SiC, and SiC/SiC composites for industries as varied as heat treatment,  
131 silicon, electronics, glass, nuclear power, and space. Figure 1 shows a  $200 \times$   
132  $200 \times 200$  portion of a synchrotron microtomograph of a sample of one of SPS's  
133 C/C composites at an incomplete densification stage (sample "CC2" in [34]).  
134 Figure 2 shows a  $200 \times 200$  slice of the microtomograph in Figure 1.



Fig. 1. A synchrotron microtomograph of a  $0.0033 \text{ mm}^3$  (side length  $< 0.15 \text{ mm}$ ) cubic sample of a C/C composite. Voxel size is  $0.745 \mu\text{m}$ .

135 Given that we are dealing with a C/C composite, there is no doubt that the

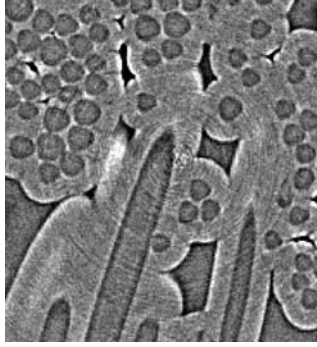


Fig. 2. A slice ( $0.0222 \text{ mm}^2$ ) of the microtomograph in Figure 1.

136 image in Figure 1 provides a very good discrimination between fibres and  
137 matrix to the human observer. The porosity typical of the CVI densification  
138 process [39–41] can also be clearly seen in the image. However, Figures 1 and  
139 2 also show a high level of noise (greylevel variations not due to differences in  
140 the material but to added noise, such that the same greylevels appear mixed  
141 in different phases), poor use of the dynamic range (few different meaningful  
142 greylevels, see below), and moderate resolution. Resolution is expected to  
143 improve in the near future. X-ray detection is performed through film or visible  
144 light scintillators, and, therefore, the system is diffraction limited. X-ray lenses  
145 to magnify the image before the detector, such as Kirkpatrick-Baez focusing  
146 devices, may overcome this limitation. Nevertheless, resolution is also limited  
147 by data bandwidth and storage capabilities.

148 However, limited resolution is not the worst characteristic of the image. Noise  
149 levels and poor quantization are. In Figure 2, apart from random noise, rings of  
150 varying intensity can be clearly seen around the tomography axis, an artefact  
151 due to variations in the efficiency of neighbouring pixels in the detector. Figure  
152 3 shows the histogram of the slice in Figure 2. Out of 256 possible levels in the  
153 8 bit quantization, only 53 have a pixel count different from zero. Moreover, 51  
154 of the 53 levels are grouped in 25 groups, thus reducing the effective dynamic



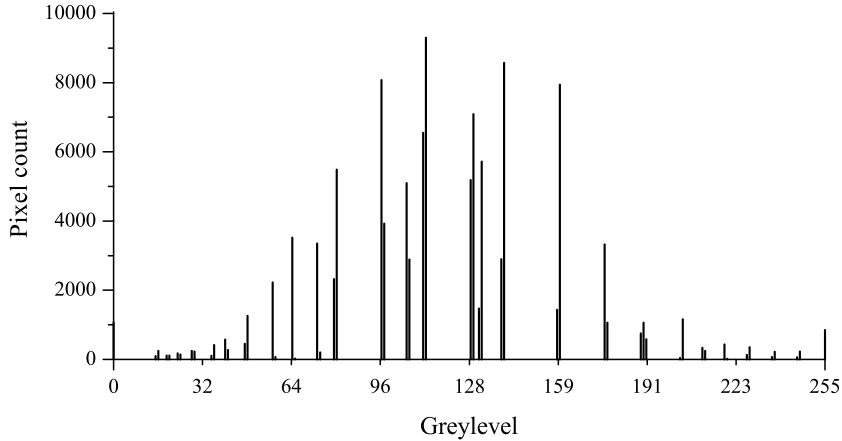


Fig. 3. Histogram of the image in Figure 2. There are 53 levels out of 256 possible levels in the dynamic range, grouped in 27 groups, thus in practice reducing the effective dynamic range to 27 levels.

155 range to 27 levels, i.e. the equivalent to less than 5 bit quantization.

156 The effect of the noise and the reduced dynamic range can be seen in the  
 157 magnified details in Figure 4. Close scrutiny reveals that, in spite of what could  
 158 be assumed from Figure 1, greyscale based per-pixel segmentation of fibres  
 159 from matrix by simple thresholding is not possible. The same grey levels are  
 160 found in all phases of the material. The human visual system is able to segment  
 161 the image because it performs high level processing involving edge detection  
 162 and pattern matching with circular/elliptical primitives [42–44] corresponding  
 163 to the expected fibre cross-sections (see the small windows at the lower right  
 164 corners). Note for instance the effect that just a sparse couple of brighter pixels  
 165 have on the recognition of the fibre in the lower right corner of the upper part  
 166 of Figure 4.

167 Within this context, our aim is to use image processing techniques for the  
 168 automated extraction of fibres and porosity from the matrix, to allow the  
 169 detailed characterization of the material.

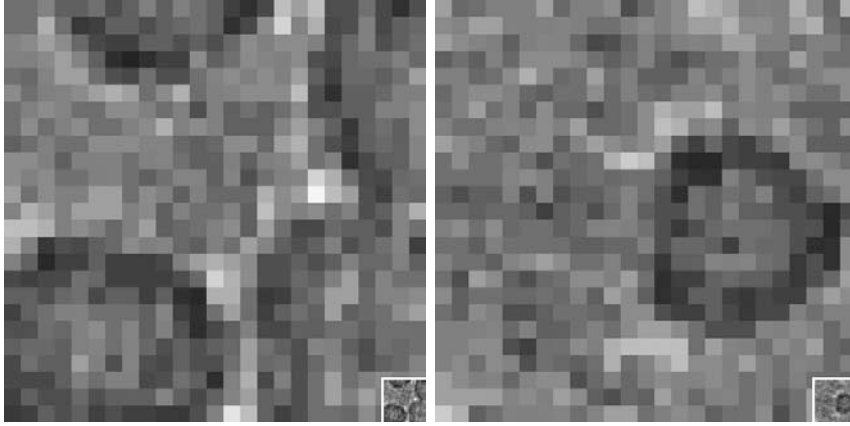


Fig. 4. Details of fibres/matrix in the image in Figure 2. The small windows at the lower right corners show the entire detail at normal scale.

### 170 **3 Method**

#### 171 *3.1 Preprocessing*

172 As we have just seen, the grey levels of individual voxels are not enough to  
173 distinguish fibre voxels from matrix voxels. It is the edges —contrast among  
174 adjacent regions in the image— that determine the boundaries of the fibres.  
175 Fibres are restituted by our visual system from the edge information. Thus, we  
176 need the edges to define the fibres in the image. We have to reduce the noise  
177 level, but any noise filtering must respect the edges. Otherwise, we would be  
178 losing the information we are seeking, the basis of the segmentation procedure.  
179 The noise has a high spatial frequency, but low pass filtering would also blur  
180 the edges. Median filtering could preserve to some extent the edges, but the  
181 resolution is too poor: The edges are too narrow as to not be wiped away  
182 by any but the smallest of filters, which would be useless. A noise reduction  
183 method capable of efficiently removing high frequency noise while preserving  
184 edges is anisotropic diffusion [45, 46].

185 Perona and Malik [45] noted that the convolution of an image  $I_0(x, y)$  with a  
 186 Gaussian kernel,

$$187 \quad K_\sigma(x, y) = \frac{1}{2\pi\sigma^2} \exp\left(-\frac{|x|^2 + |y|^2}{2\sigma^2}\right) \quad (1)$$

188 with standard deviation  $\sigma$  yields the same result as the solution of the isotropic  
 189 diffusion (heat) partial differential equation,

$$190 \quad \frac{\partial I(x, y, t)}{\partial t} = \text{div}(\nabla I(x, y, t)), \quad (2)$$

191 where  $I(x, y, t)$  is the image  $I(x, y)$  at time  $t = 0.5\sigma^2$ , with initial conditions  
 192  $I(x, y, 0) = I_0(x, y)$ , and  $\nabla I$  is the image gradient.

193 Introducing in (2) as *diffusion conductance* or *diffusivity*,  $g(s)$ , a rapidly de-  
 194 creasing function of a greyscale edge detector such as the gradient magnitude,  
 195  $s = |\nabla I|$ ,

$$196 \quad \frac{\partial I(x, y, t)}{\partial t} = \text{div}(g(|\nabla I(x, y, t)|)\nabla I(x, y, t)), \quad (3)$$

197 smoothing on both sides of edges becomes much stronger than across them. A  
 198 diffusivity constant with time but varying with location  $(x, y)$  would make (2)  
 199 a linear nonhomogeneous diffusion equation. However, if  $g$  is made a function  
 200 of time, as in (3), the diffusion equation becomes nonlinear and nonhomo-  
 201 geneous, referred to as *anisotropic* in the image processing literature, even  
 202 when conventional PDE terminology reserves the term for the case where the  
 203 diffusivity is a tensor, varying both with location and direction. The conse-  
 204 quence of this “pseudoanisotropy” is that only the magnitude but not the  
 205 direction of the diffusion flux can be controlled. Noise close to edges remains  
 206 unchanged due to the small flux in the vicinity of edges. To enable smoothing

207 parallel to edges, (3) must be generalized with a diffusivity matrix  $G$  with  
 208 nonzero off diagonal elements (see, for instance, [46–50]), thus rendering it  
 209 truly anisotropic.

210 Perona and Malik suggested

$$211 \quad g(s) = \frac{1}{1 + s^2/\kappa^2} \quad (4)$$

212 and

$$213 \quad g(s) = \exp(-s^2/\kappa^2) \quad (5)$$

214 as diffusivity functions. Since then, many other diffusivity functions have been  
 215 proposed [46, 51]. In fact, Black *et al.* [51] demonstrated that anisotropic dif-  
 216 fusion in the sense of (3) is the gradient descent of an estimation problem  
 217 with a robust error norm induced by  $g(s)$ , thus providing a sound theoretical  
 218 foundation to choose adequate diffusivity functions.

219 As several authors have revealed [52–55], (3) is an ill-posed problem, in the  
 220 sense that images close to each other are likely to diverge during the process [54],  
 221 but it can be stabilized by regularization. One common approach [53] is to  
 222 smooth the variable of the diffusivity, i.e. to use a smoothed version of the  
 223 image for the gradient in each step, as in

$$224 \quad \frac{\partial I(x, y, t)}{\partial t} = \operatorname{div}(g(|\nabla I_\sigma(x, y, t)|)\nabla I(x, y, t)), \quad (6)$$

225 where  $I_\sigma = K_\sigma * I$ , with  $K_\sigma$  a suitable local convolution kernel of width  $\sigma$ , for  
 226 instance a Gaussian kernel. However, Weickert and Benhamouda [56] proved  
 227 that a standard spatial finite difference discretization is sufficient to turn (3)  
 228 into a well posed system of nonlinear ordinary differential equations. Therefore,

229 direct implementations of the Perona-Malik filter tend to work reasonably well  
 230 because of the regularizing effect of the discretization.

231 The extension to  $D$  dimensions is straightforward. The diffusion process is  
 232 described by the equation

$$233 \quad \frac{\partial I(\mathbf{x}, t)}{\partial t} = \operatorname{div}(G \cdot \nabla I(\mathbf{x}, t)), \quad (7)$$

234 where  $\mathbf{x} \in \mathbb{R}^D$  and  $G$  is a square  $D \times D$  diffusivity matrix. Equation (3) is (7)  
 235 with  $G$  a diagonal  $2 \times 2$  matrix with equal diagonal elements  $g(|\nabla I|)$ . Diffusion  
 236 filtering is usually implemented using simple finite differences to approximate  
 237 the image derivatives within an explicit or Euler-forward scheme.

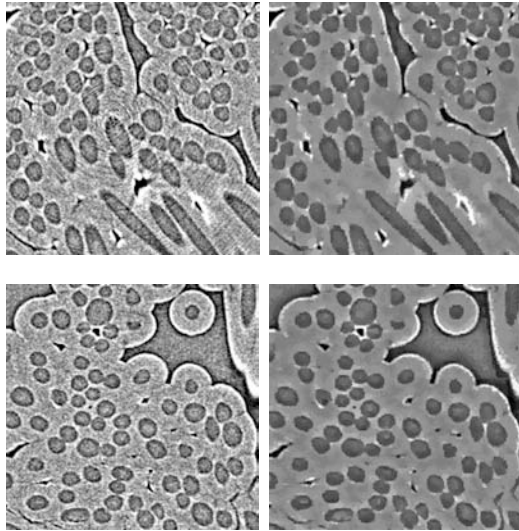


Fig. 5. Two orthogonal slices of the tomograph in Figure 1 before (left) and after (right) filtering with 3D anisotropic diffusion.

238 Figure 5 shows the results of applying (7) with (4) and  $D = 3$  to the tomograph  
 239 in Figure 1, and they are quite satisfactory. The relevant edges have been  
 240 preserved while most of the noise has been wiped away. Note that the filter is  
 241 equally efficient on the two types of noise present in the image, the random  
 242 uniform noise and the circular patterns around the tomography axis.

244 However good the results in Figure 5 regarding noise reduction and mesoscale  
 245 feature preservation, fibres cannot yet be separated on the basis of individual  
 246 voxel grey levels. Many fibres show brighter nuclei inside darker boundaries,  
 247 whose grey levels can also be encountered in the matrix. Our approach is  
 248 masking all pixels within edges. For that purpose we use a differential profiler  
 249 [57] along voxel rows. A differential profile is obtained by constructing an  
 250 array of integers where every element represents the lowpass filtered gradient  
 251 of the grey levels along a scan line. This is easily implemented using exclusively  
 252 integer arithmetic. Let  $I_{x,y,z}$  be the greyscale image. Let  $P_l$  be an integer vector  
 253 to hold the profile of a scan line, and assume without loss of generality that  
 254 the scan direction is along  $+x$ . Combining forward differencing

$$255 \quad P_l = I_{l,y,z} - I_{l+1,y,z} \quad (8)$$

256 with lowpass filtering

$$257 \quad P_l = \frac{1}{3}(P_{l-1} + P_l + P_{l+1}), \quad (9)$$

258 and forgetting about the dividing constant, we get

$$\begin{aligned} P_l &= I_{l-1,y,z} - I_{l,y,z} + I_{l,y,z} \\ &\quad - I_{l+1,y,z} + I_{l+1,y,z} - I_{l+2,y,z} \\ &= I_{l-1,y,z} - I_{l+2,y,z} \end{aligned} \quad (10)$$

259 and thus the whole procedure to obtain the profile is reduced to a sequence  
 260 of integer subtractions of grey levels. Near-zero profile segments reflect parts  
 261 of the image where no significant variations of grey level occur. Positive peaks  
 262 reflect decreasing grey levels, such as when entering a fibre, and negative peaks

263 increasing bright, such as when leaving a fibre. The narrower the peak, the  
 264 faster the variation. The higher the peak, the greater the variation. Thus,  
 265 peak shape and magnitude tell us everything we need to know about intensity  
 266 transitions along a given direction.

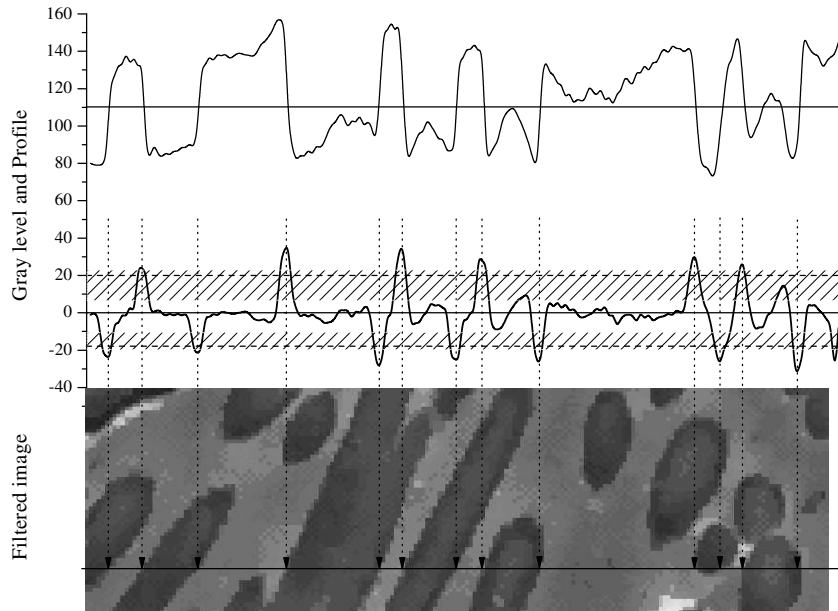


Fig. 6. Edge detection by profiling scan lines in slices of the tomograph in Figure 1 after filtering with 3D anisotropic diffusion. The patterned areas in the profile graph show the range of possible thresholds for successful detection of all fibres in the given line.

267 Figure 6 shows a grey level profile (above) and the corresponding differential  
 268 profile (center) along a line of the tomograph in an arbitrary direction (below).  
 269 A tentative grey level threshold is plotted on the grey level profile (upper  
 270 graph), to show the lack of robustness of a per-pixel approach due to the  
 271 brighter nuclei of some fibres. The vertical arrows show the edges in the image  
 272 corresponding to the peaks above or below tuneable thresholds (dashed lines)  
 273 in the differential profile (lower graph). The range of possible thresholds that  
 274 would achieve successful detection of all fibre edges in the line is highlighted

275 in the graph. The upper (in absolute value sense) bounds for the thresholds  
276 are dictated by two criteria: 1) The positive threshold should be low enough  
277 as to not miss any positive peak at the entrance of a fibre, and 2) the negative  
278 threshold should not miss any negative peak at the exit of a fibre. The lower  
279 bound for the positive threshold depends only on the peaks outside fibres  
280 (positive peaks inside fibres are irrelevant): the threshold should not allow  
281 any peak not lying at the entrance of a fibre. Conversely, the lower bound for  
282 the negative threshold depends only on the peaks inside fibres (negative peaks  
283 outside fibres are irrelevant): the negative threshold should be high enough as  
284 to exclude any negative peak not at the exit of a fibre.

285 To obtain a mask of fibre voxels, therefore, the voxel rows along the three  
286 possible orientations in the 3D image are profiled, such that all voxels along  
287 a differential profile from a positive peak to a negative peak are marked as  
288 foreground voxels, and the rest as background voxels. In the resulting mask,  
289 some fibres are “broken”, i.e. the dark boundary does not surround the entire  
290 fibre, and therefore some profiles may result in spurious rectilinear spikes pro-  
291 truding from the fibre mask, due to the lack of a negative peak, or well similar  
292 rectilinear structures may be missing from the interior of a fibre due to the  
293 lack of a positive peak, or a spurious negative peak with sufficient magnitude  
294 inside a fibre.

295 Here is where spatial correlation among the different orientations in the 3D  
296 image enters, as interior fibre voxels not marked in a profile in a given direction  
297 are likely to be marked in the profiles along any of the transversal directions,  
298 and thus the *a priori* knowledge of the morphology of the fibres is enough, in a  
299 simple postprocessing stage, to get rid of the majority of the thin, rectilinear,  
300 spike-like 2D artifacts protruding from or entering “broken” fibres.



301 Porosity in the matrix is segmented by the same procedure, only the thresholds  
302 for the peak detection in the differential profile are tuned to the characteristic  
303 edges of the porosity regions, where transitions are more pronounced than in  
304 fibres, see the darker lacunar areas with a brighter rim in Figure 5. This is  
305 due to the contrast saturation effect in the matrix/air interface induced by  
306 the increased sensitivity of the tomograph in order to resolve carbon/carbon  
307 interfaces.

308 Both the fibre and the porosity masks can be “cleaned” with a labelling al-  
309 gorithm if their inspection reveals it to be necessary. Cleaning the masks con-  
310 sists in getting rid of remnants of matrix material that may be adhered to the  
311 outside face of fibre or porosity boundaries due to imprecisions in the exact  
312 localization of edges. This is achieved by 1) labelling all connected foreground  
313 voxels in the mask (fibres or porosity) with a unique label subject to the  
314 condition of their original grey levels being below a given threshold, and 2) la-  
315 belling as background voxels (i.e. delete from the mask) all connected groups  
316 of remaining unlabelled voxels in the mask if any voxel in the group touches  
317 a background voxel (matrix). This ensures that the “bright voxel hunt” takes  
318 effect only in groups of voxels attached to the exterior boundary of fibres or  
319 porosity, without affecting the bright cores of fibres. The result is a purified  
320 mask of fibre or porosity voxels where bright voxels are only permitted in the  
321 interior of fibres.

322 The masks thus obtained, see Figure 7 and Figure 8 for some partial render-  
323 ings of fibre bundles and porosity, can be combined into a unique material  
324 description mask, detailing the microstructure of the material. All voxels in  
325 the tomograph are classified as belonging to one of the three phases in the  
326 material: matrix, fibre, or porosity. This mask can then be directly fed into

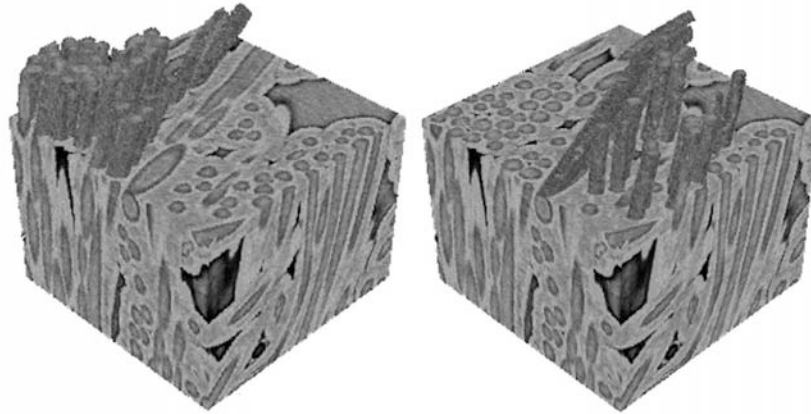


Fig. 7. Partial renderings of some fibre bundles, using the original grey levels in the tomograph.

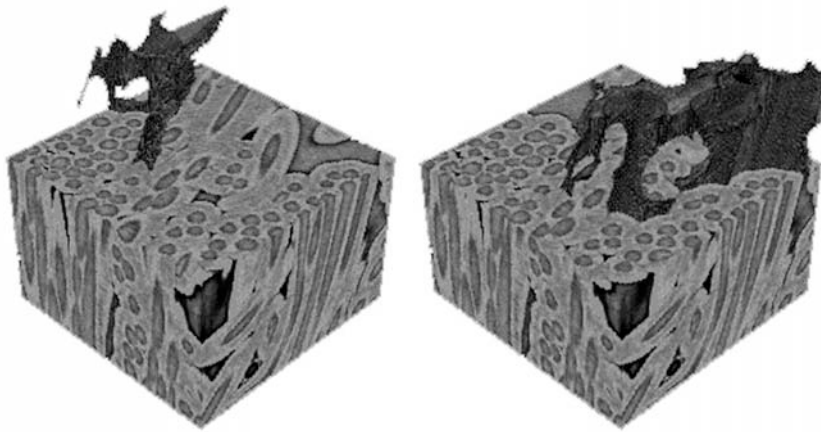


Fig. 8. Partial renderings of the porosity formed during the CVI process, using the original grey levels in the tomograph.

327 models requiring a precise description of the microstructure of the material.  
328 Thus, for instance, a Finite Element Model can be constructed just by assim-  
329 ilating the finite elements to the classified voxels.

### 330 *3.3 Fibre individuation: The heavy ball*

331 The microstructure of the sample is contained in the mask, indeed, but still  
332 some further processing is necessary in order to be able to perform a com-

333 plete characterization of the microstructure. Some usual characteristics, such  
334 as void content or volume fractions, can be directly computed from the phase  
335 masks. However, others not less important such as the distribution of fibre  
336 lengths, orientations, curvature, or waviness, cannot. Fibres have to be identi-  
337 fied individually in order to be able to measure individual characteristics such  
338 as those just mentioned.

339 A connected component labelling algorithm could do it, if we could warrant  
340 that individual fibres do not touch each other in the mask. However, this is not  
341 the case. Fibres touch each other both because of the limited resolution of the  
342 image and because some of them actually touch each other in the material.  
343 Therefore a connected component algorithm is able only to separate fibre  
344 bunches, groups of fibres either touching each other or close enough as to not  
345 be resolved by the spatial resolution of the imaging system, see Figure 7.

346 We use a novel method, the *heavy ball*, to successfully separate individual  
347 fibres. It treats the fibre mask as a solid block drilled by wormholes, the  
348 fibres. The hole mouths are located in each side of the block, and a zero drag,  
349 zero gravity, high inertial ball is pushed into each hole in turn. The ball size is  
350 adapted to the diameter of each hole. The ball is forced to move continuously  
351 until it either finds the end of the fibre or leaves the block. The ball run along  
352 each fibre can be used to label the fibre with a unique identifier for subsequent  
353 characterization, or directly to compute the required parameters.

354 For locating the ball entrance points and estimating the required ball size,  
355 the ellipse fitting procedure depicted in [20, 58], see [59], is applied to each  
356 outer boundary (six 2D binary images) of the binary fibre mask. The method  
357 requires the labelling of the connected components in each boundary. During

358 the labelling, the centroid and the covariance matrix of the coordinates of the  
 359 pixels in each connected component is computed. The centroid (average loca-  
 360 tion) gives the center of the fitted ellipse, and the root of the lesser eigenvalue  
 361 of the covariance matrix  $\Sigma$  gives its minor axis, which coincides with the fibre  
 362 radius,  $r$ :

$$363 \quad r^2 = 2(\Sigma_{11} + \Sigma_{22} - \sqrt{\Delta}), \quad (11)$$

364 where

$$365 \quad \Delta = (\Sigma_{11} + \Sigma_{22})^2 - 4(\Sigma_{11}\Sigma_{22} - \Sigma_{12}\Sigma_{21}). \quad (12)$$

366 Touching fibres in the 2D image have to be split before the ellipse fitting  
 367 procedure. Otherwise a single enclosing ellipse will be fitted to an entire group  
 368 of touching fibres in the 2D image. The splitting of touching fibres can be  
 369 performed by means of mathematical morphology operators, using successive  
 370 erosions and dilations, such that fibres are shrunk until disconnection and  
 371 then expanded again constrained to the original image. Disconnecting touching  
 372 groups of pixels is a well known application of mathematical morphology [22].

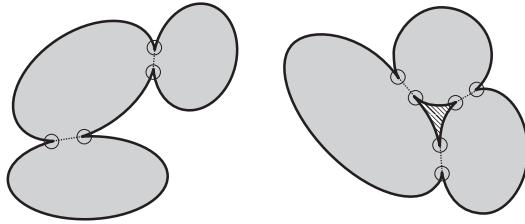


Fig. 9. Ellipse splitting procedure: left) Simple case; right) Complex case not consid-  
 ered in [58]. Small circles mark convex perimeter points. Dotted lines mark splitting  
 lines. The greyed area within the group on the right is enclosed by an internal  
 perimeter.

373 An alternative approach is described in [58]. The perimeters —foreground

374 pixels with at least one background neighbour— of the connected components  
375 in the 2D images are sequentially traversed and their curvature computed at  
376 each perimeter pixel. Pixels where the curvature becomes convex are recorded.  
377 If two fibres touch each other, there will be two convex points. A straight line  
378 joining the points can be drawn to split the fibres, so they can be labelled  
379 as two different components. If three or more fibres touch, it could be just  
380 a trivial extension of the two-fibre case, and then a line is drawn for each  
381 consecutive pair of convex points, see Figure 9 (left). However, it could also  
382 be a special case, not considered in [58], where three or more fibres touch  
383 each other, thus totally enclosing a background region inside the group, see  
384 Figure 9 (right). In this case, an odd number of convex points is found when  
385 traversing the external perimeter of the group. If this is the case, the internal  
386 perimeter (the perimeter of the enclosed background) has to be traced also,  
387 and the splitting lines should be drawn between pairs formed by a convex  
388 point from the external perimeter and the closest convex point in the internal  
389 perimeter, see Figure 9 (right). As many convex points have to be found in  
390 the internal perimeter as in the external perimeter. If they are not, another  
391 background area is enclosed within the group, and so on.

392 Therefore, if the aggregation pattern of the fibres in a given sample is not  
393 too complex, the convex point search is probably faster than mathematical  
394 morphology. Otherwise, mathematical morphology is probably a safer choice.  
395 No matter what method is used, splitting the touching fibres is a fast opera-  
396 tion. Note that it is only performed on the external sides of the 3D domain  
397 of the fibre mask,  $\mathcal{M}_f$ , six 2D binary images. Moreover, the purpose of ellipse  
398 fitting is locating entrance points for the heavy ball, and this is performed  
399 sequentially. Fibres traversed from the first side are likely to emerge on any

400 of the sides. Fibres are marked as they are traversed, to avoid repeated runs.  
 401 Thus, as the process progresses through the sides, each side has less and less  
 402 ellipses left to be fit.

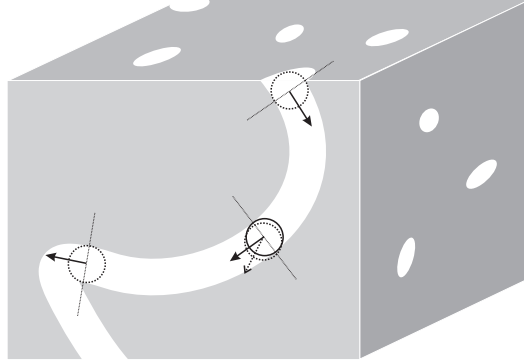


Fig. 10. Identification of individual fibres with the heavy ball method. Solid arrows show the direction of the previous move. The dotted arrow and circle represent a candidate movement. The thinner dotted line marks the limit for candidate moves depending on the previous move. Ellipses in the mask surface are best fits to the fibre sections and determine the radius and initial location of the ball.

403 Once the center and radius of the “wormhole” have been estimated, a heavy  
 404 ball of the appropriate size —same radius as the fibre, i.e. minor axis of the  
 405 fitted ellipse,  $r$ , equation 11— is placed centred in the hole mouth. Figure 10  
 406 illustrates the method. The ball has inertia, i.e. at step  $k$  it remembers the  
 407 previous move, vector  $\mathbf{m}^k$ . This memory is initialized opposite to the normal of  
 408 the current mask boundary,  $\mathbf{m}^0 = -\hat{\mathbf{n}}$ . The ball moves looking for the widest  
 409 passage, one voxel at a time. The set of candidate locations for the centre of  
 410 the ball,  $\mathcal{C}^k$ , is made of all the voxels  $C_i$  adjacent to the current centre  $C^k$   
 411 such that the direction of advance is at most at right angles with the previous  
 412 movement. This is verified by means of the scalar product of the vector of the

413 previous move and the vector linking the current centre and the candidates:

$$414 \quad \mathcal{C}^k = \left\{ C_i \in \mathcal{M}_f \mid \|\overline{C^k C_i}\|_0 = 1 \wedge \overline{C^k C_i} \cdot \mathbf{m}^k \geq 0 \right\} \quad (13)$$

415 For each step, the number  $s(C_i)$  of fibre voxels overlapped by the ball in each  
416 candidate location  $C_i$  is computed:

$$417 \quad \mathcal{O}_i^k = \left\{ P \in \mathcal{M}_f \mid f(P) = 1 \wedge \|\overline{C_i P}\|_2^2 \leq r^2 \right\} \quad (14)$$

$$418 \quad s(C_i) = I(\mathcal{O}_i^k) \quad (15)$$

419 where  $f : \mathcal{M}_f \subset \mathbb{Z}^3 \rightarrow \{0, 1\}$  is the binary fibre mask.

420 If the maximum overlap is verified for more than one candidate location, the  
421 one closest to the previous direction is chosen, i.e. the one maximizing the  
422 scalar product of the intended and the previous movement:

$$423 \quad C^{k+1} = \arg \max_{C_i \in \mathcal{C}^k} \left\{ s(C_i) \wedge \overline{C^k C_i} \cdot \mathbf{m}^k \right\} \quad (16)$$

424 This step by step advance is repeated until the centre of the ball leaves the  
425 fibre, either because the fibre ended inside the mask, or because the ball is  
426 leaving the mask,  $C^k \notin \mathcal{M}_f$ .

427 During the advance of the ball the centre locations  $\{C^k\}$  can be recorded  
428 —for instance for a curvature analysis—, the length of the moves accumu-  
429 lated,  $\sum_k \|\mathbf{m}^k\|_2$ , —to estimate the length of the fibre—, the fibre voxels  $\cup \mathcal{O}^k$   
430 labelled with a unique identifier —for further characterization in a later occa-  
431 sion or involving several fibres, such as nearest neighbour and average distance  
432 computations—, and appropriate statistics can be computed, such as extreme  
433 locations of the fibre centres  $\{C^k\}$ , or variations in the fiber width or size

434 by inspection of the cross sections at right angles with the current movement  
435 vector,  $\mathbf{m}^k$ .

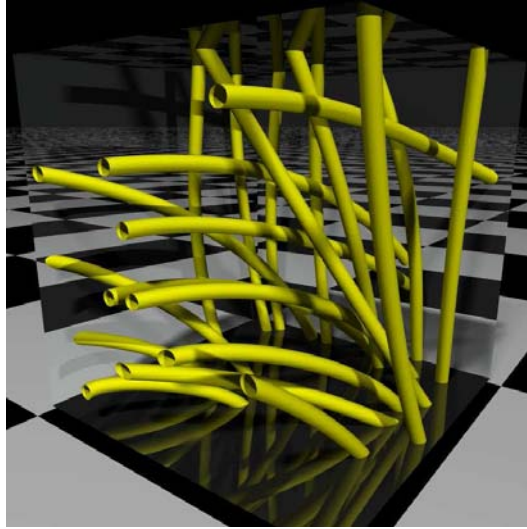


Fig. 11. Rendering of some of the fibres in the sample in Figure 1 after separation with the heavy ball. Only some fibres are shown to avoid visual clutter.

436 Figure 11 shows some isolated fibres in the sample in Figure 1, where the  
437 output of the heavy ball algorithm has been used to produce a ray tracing  
438 rendering.

### 439 *3.4 Labelling algorithms*

440 Several steps in the methodology depicted above use connected components  
441 labelling algorithms, both in 2D and 3D.

442 2D labelling is required for the ellipse fitting procedure. The components tar-  
443 geted by the algorithm are, if the previous processing was successful, small to  
444 medium compact rounded shapes. Here the simple classical recursive labelling  
445 algorithm [60, 61], also known as region growing or region burning, is likely  
446 to work fast and well. Moreover, the labelling aims at computing moments of



447 each connected component, and this can be easily done during the labelling  
448 with the recursive method. The limited size of the components is likely to pre-  
449 vent any stack overflow problem arising from its recursive nature, the cause  
450 why it is usually discarded in benefit of the two-pass iterative algorithm.

451 In the classical two-pass iterative method [62,63], first the image is traversed  
452 in raster scan order assigning temporary labels to the components, and then  
453 a second pass resolves conflicts in components with multiple labels, thus re-  
454 quiring an equivalence table to record label conflicts, usually handled with  
455 a Union-Find data structure [64]. Therefore, in exchange of the robustness  
456 implicit in its iterative nature, it is far more complex than the recursive algo-  
457 rithm, and characterizing components during the labelling is not straightfor-  
458 ward, as components are not labelled sequentially and labels are not resolved  
459 until the second pass.

460 Recently a hybrid algorithm has been proposed [65,66], that has proven to  
461 be faster and more robust for compact objects than the classical recursive  
462 algorithm, whereas maintaining its simplicity and versatility. The 2D labelling  
463 in the ellipse fitting procedure is therefore a good instance for adoption of the  
464 hybrid technique.

465 3D labelling is used to purify the phase mask. Labelling in 3D, however, can  
466 be trickier. The components are not moderately sized anymore. We are dealing  
467 now with three dimensions, and the recursion depth and the required stack  
468 grow accordingly. Thus serious doubts arise about the robustness of the algo-  
469 rithms relying on recursion. The classical recursive algorithm can be rewritten  
470 in iterative form, by using a custom stack. However, this comes at the cost of  
471 increased complexity.

	Rec. depth		Time (ms)	
<b>Recursive</b>	281 607		146.9	+62%
<b>Iterative</b> (Stack)	252 341	89.6%	167.3	+84%
<b>Hybrid along <math>x</math></b>	27 617	9.8%	108.9	+20%
<b>Hybrid along <math>y</math></b>	26 246	9.3%	99.7	+10%
<b>Hybrid along <math>z</math></b>	15 481	5.5%	90.9	
<b>Two-pass</b>	N/A	N/A	497.8	$\times 5.5$

Table 1

Performance data in the labelling of the fibre mask with different labelling algorithms.

472 We analyzed the performance and robustness in 3D of the different alternatives  
473 in the labelling of the phase mask. Table 1 summarizes the results, including  
474 different scan directions for the hybrid algorithm, which is anisotropic, in the  
475 sense that it favours a direction of choice. Note the effect of the inherent  
476 anisotropy of the fibrous components, even when many fibres in the sample  
477 deviate significantly from the main orientation,  $z$ , specially towards  $y$ , see  
478 Figure 11 and axes in Figure 1. All data were obtained on a iPentium M 2.13  
479 GHz, 1 GByte RAM, OS MS WindowsXP. Both time and stack figures were  
480 clearly favourable to hybrid labelling. A detailed analysis can be found in [66].

#### 481 4 Discussion

482 The study case accompanying the description of the method just described  
483 shows its effectivity. It deals with a sample showing all the problems typical of

484 a C/C composite synchrotron tomograph, and demonstrates how the method  
485 is able to tackle them and results in a detailed description of the microstructure  
486 of the sample, either in the form of a phase mask suitable for numerical models  
487 working on explicit spatial domains, or up to the point of a detailed individual  
488 characterization of each fibre in the sample. Specifically, the heavy ball is not  
489 only able to separate the fibres, but it also produces a set of data permitting a  
490 whole range of measurements, from simple statistics, such as fibre length and  
491 orientation, to the parameterization of fibres as 3D curves, surfaces, or solids,  
492 see Figure 11.

493 With respect to the computational overhead, clearly the heaviest stage is the  
494 anisotropic diffusion filtering. Completing the 30 to 40 iterations needed to  
495 get results such as those in Figure 5 on the  $200^3$  sample takes several minutes.  
496 However, techniques do exist capable of accelerating significantly anisotropic  
497 diffusion [67].

498 The differential profiler is very fast, the whole procedure in all sections along  
499 the three directions, including the correlation stage, takes about 2 seconds.

500 With respect to the stages involving labelling algorithms, time figures are pro-  
501 vided in the previous section, and a detailed analysis of these techniques can  
502 be found in [65,66]. If the right choice is made in the selection of the labelling  
503 algorithm, labelling times for moderately sized samples are very small. How-  
504 ever, it should be noted that, in spite of the high reduction in stack overhead  
505 of the hybrid technique, it still uses recursivity, and this could be a source  
506 of trouble as sample sizes grow. For the 3D labelling of big samples, it may  
507 be necessary to resort to block techniques, where the sample is labelled by  
508 blocks [68], or to use an iterative technique.

509 Regarding the heavy ball, computation time depends on the length and radius  
510 of the fibre, but the average fibre, 200 voxel long and 14 voxel in diameter,  
511 takes about 60 ms, including dumping the center locations to a text buffer  
512 for export. Future implementations of the algorithm can yet be optimized  
513 for speed, for instance by avoiding repeated computations in the overlap for  
514 candidate moves at each step.

515 With respect to parametric complexity, tuneable parameters are only found  
516 in two of the stages, the preprocessing filtering and the differential profiler.  
517 Anisotropic filtering uses three parameters, the noise scale  $\sigma$  in (6), the feature  
518 scale  $\kappa$  in (4), and the number of iterations. These usually require careful fine  
519 tuning when dealing with applications related to enhancement of images with  
520 multiple levels of detail and where the visual appearance of the final result  
521 is a major factor. However, 1) in our case the noise scale and the feature  
522 scale are well defined and well apart, and 2) we use anisotropic diffusion to  
523 provide suitable input for the differential profiler, which has a high degree of  
524 robustness and is itself tunable.

525 The result is that, as long as the noise is sufficiently eliminated and the  
526 mesoscale features of the microstructure are well preserved, the sensitivity to  
527 the parameters of the diffusion filter is very low. Differences among parameter  
528 configurations can be handled by the tuneable thresholds in the differential  
529 profiler. We recommend plotting a couple of profiles anywhere through the  
530 sample every, say, ten iterations of the anisotropic diffusion filter, so that the  
531 progress in the edge enhancement and noise reduction can be tracked, a suit-  
532 able stopping point for the diffusion can be chosen, and adequate thresholds  
533 for the profiler can be set.

534 Regarding precision, anisotropic diffusion has the interesting property of pre-  
535 serving not only the existence of edges at the feature scale, but also their  
536 location. With the differential profiler, on the other hand, it is possible to de-  
537 termine with high accuracy the position of edges, and also to choose the outer  
538 side of the features (first threshold crossing point for ‘entry’ peaks and second  
539 for ‘exit’ peaks), the inner side (vice versa), or exactly the edge (maximum  
540 between threshold crossing points), see Figure 6.

541 The only potential source of trouble are brighter cores within the fibres which  
542 sometimes may percolate to the outside of the fibre through a broken edge,  
543 creating a connection with the matrix material and leaving a gap for the  
544 differential profiler. However, correlations among profiles in the three spatial  
545 directions decrease their probability, and, moreover, the path of the heavy ball  
546 is not likely to be affected by these spots. Nevertheless, in significant numbers  
547 they could affect some of the statistics. An inspection of the phase mask will  
548 reveal the extent of the problem, if any, and advice about the opportunity  
549 of a finer tuning of the profiler thresholds or the anisotropic diffusion before  
550 characterization.

551 Note also that the procedure described for the application of the heavy ball  
552 would miss any fibre entirely embedded *inside* the sample. If a low but signif-  
553 icant probability of short fibres entirely embedded in the sample is expected,  
554 the interior of the fibre mask may be scanned after completing the procedure,  
555 looking for fibre voxels that were not tracked by the heavy ball, in order to  
556 apply it there. Alternatively, if the material is expected to have a large pro-  
557 portion of short (with respect to sample size) fibres, the heavy ball can be  
558 applied as if peeling an onion: first the heavy ball is applied to all six outer  
559 boundaries of the sample, then the procedure is repeated a little deeper into

560 the sample for any fibre section not yet tracked, and so on, until the volume  
561 being inspected is too small as to contain any fibres.

562 Finally, note that the diffusion process in the preprocessing stage involves  
563 mixing contributions from neighbouring voxels. This implies the existence of  
564 border effects near the image boundaries. Edge detection in the profiler, in  
565 turn, uses finite differences involving separated voxels, and it is not able to  
566 detect edges if they are just at the boundary of the image. Moreover, in the  
567 correlation among profiles, the extreme ends of profiles count with much less  
568 information than the rest. All this added up results in the outer boundaries of  
569 the resulting mask having a high degree of unaccuracy in the determination  
570 of phase type. Therefore, it is a good practice to discard a few layers of voxels  
571 around the mask before any further processing.

## 572 **5 Conclusion**

573 We have detailed and illustrated a multistage methodology able to extract and  
574 characterize the true microstructure of a fibrous C/C composite using phase  
575 contrast X-ray microtomography. Since C/C composites are probably a worst-  
576 case benchmark, the method can also be applied to other cylindrical fibre  
577 composites. The processing chain is made of 1) a preprocessing stage where  
578 3D anisotropic diffusion filtering is used to reduce the noise while preserving  
579 the features in the sample; 2) a differential profiling method to detect areas  
580 between intensity edges on every 2D cross section parallel to the reference  
581 system, which are then refined by correlating the outputs in 3D; 3) an optional  
582 “cleaning phase” using a 3D labelling algorithm to purify the resulting mask;  
583 and 4) a novel fibre separation process which requires an ellipse fitting procedure

584 applied to the outer boundaries of the 3D mask followed by the use of what  
585 we call a heavy ball to individually identify each fibre and characterize it.

586 We hope to have contributed to demonstrate the ability of phase contrast  
587 X-ray tomography to produce sufficient information as to extract the true  
588 microstructure of composites with constituents with close densities, such as  
589 C/C composites, when appropriate image processing techniques are used.

## 590 **Acknowledgements**

591 The authors wish to thank Prof. G. L. Vignoles and O. Coindreau (LCTS),  
592 Snecma Propulsion Solide, and the ESRF (European Synchrotron Radiation  
593 Facility) ID 19 team for providing us with the C/C composite 3D image.

## 594 **References**

- 595 [1] Fakirov S, Fakirova C. Direct determination of the orientation of short glass  
596 fibers in an injection-molded poly(ethylene terephthalate) system. *Polym*  
597 *Compos.* 1985;6:41–46.
- 598 [2] Bay RS, Tucker III CL. Stereological measurement and error estimates for  
599 three-dimensional fibre orientation. *Polym Eng Sci.* 1992;32(4):240–253.
- 600 [3] Fischer G, Eyerer P. Measuring the spatial orientation of short fibre reinforced  
601 thermoplastics by image analysis. *Polym Compos.* 1988;9(4):297–304.
- 602 [4] Wetherhold RC, Scott PD. Prediction of thermoelastic properties in short-  
603 fiber composites using image analysis techniques. *Compos Sci Technol.*  
604 1990;37(4):393–410.

- 605 [5] Clarke AR, Davidson NC, Archenhold G. Measurements of fibre directions in  
606 reinforced polymer composites. *J Microsc (Oxford)*. 1993;171:69–79.
- 607 [6] Guild FJ, Summerscales J. Microstructural image analysis applied to fibre  
608 composite materials: a review. *Composites*. 1993;24:383–393.
- 609 [7] Paluch B. Analysis of geometric imperfections in unidirectionally-reinforced  
610 composites. In: *Proceedings of the European Conference on Composite  
611 Materials (ECCM6)*; 1993. p. 305–310.
- 612 [8] Mattfeldt T, Clarke AR, Archenhold G. Estimation of the directional  
613 distribution of spatial fibre processes using stereology and confocal scanning  
614 laser microscopy. *J Microsc (Oxford)*. 1994;173(2):87–101.
- 615 [9] Clarke AR, Archenhold G, Davidson NC. A novel technique for determining  
616 the 3D spatial distribution of glass fibres in polymer composites. *Compos Sci  
617 Technol*. 1995;55:75–91.
- 618 [10] Paluch B. Analysis of geometric imperfections in unidirectional reinforced  
619 composites. *J Compos Mater*. 1996;30(4):454–485.
- 620 [11] Davidson NC, Clarke AR, Archenhold G. Large-area, high-resolution image  
621 analysis of composite materials. *J Microsc (Oxford)*. 1997;185(2):233–242.
- 622 [12] Joyce PJ, Kugler D, Moon TJ. A technique for characterizing process induced  
623 fiber waviness in unidirectional composite laminates using optical microscopy.  
624 *J Compos Mater*. 1997;31(17):1694–1734.
- 625 [13] Zhu YT, Blumenthal WR, Lowe TC. Determination of non-symmetric 3-D fiber-  
626 orientation distribution and average fiber length in short-fiber composites. *J  
627 Compos Mater*. 1997;31(13):1287–1301.
- 628 [14] Clarke AR, Archenhold G, Davidson NC. 3D Confocal microscopy of glass  
629 fibre reinforced composites. In: Summerscales J, editor. *Microstructural*



- 630 Characterisation of Fibre-Reinforced Composites. Cambridge: Woodhead  
631 Publishing; 1998. p. 55–137.
- 632 [15] Mlekusch B. Fibre orientation in short-fibre-reinforced thermoplastics  
633 II: Quantitative measurements by image analysis. *Compos Sci Technol.*  
634 1999;59:547–560.
- 635 [16] Zak G, Park MHCB, Benhabib B. Estimation of average fibre length in short-  
636 fibre composites by a two-section method. *Compos Sci Technol.* 2000;60:1763–  
637 1772.
- 638 [17] Eberhardt CN, Clarke AR. Fibre orientation measurements in short glass  
639 fibre composites. Part I: automated, high-angular resolution measurement by  
640 confocal microscopy. *Compos Sci Technol.* 2001;61:1389–1400.
- 641 [18] Vignoles GL. Image segmentation for hard X-ray phase contrast images of C/C  
642 composites. *Carbon.* 2001;39:167–173.
- 643 [19] Lee YH, Lee SW, Youn JR, Chung K, Kang TJ. Characterization of fiber  
644 orientation in short fiber reinforced composites with an image processing  
645 technique. *Mater Res Innov.* 2002;6:65–72.
- 646 [20] Blanc R, Germain C, Da Costa JP, Baylou P, Cataldi M. Fiber orientation  
647 measurements in composite materials. *Compos Pt A-Appl Sci Manuf.*  
648 2006;37:197–206.
- 649 [21] Clarke AR, Eberhardt CN. *Microscopy Techniques for Materials Science.*  
650 Cambridge: Woodhead Publishing; 2002.
- 651 [22] Gonzalez RC, Woods RE. *Digital Image Processing.* 2nd ed. Upper Saddle  
652 River, NJ: Prentice Hall; 2002.
- 653 [23] Wilson T. *Confocal Microscopy.* London: Academic Press; 1993.

- 654 [24] Russ JC, Dehoff RT. Practical Stereology. 2nd ed. New York: Plenum Press;  
655 2000.
- 656 [25] Sterio DC. The unbiased estimation of number and sizes of arbitrary particles  
657 using the dissector. *J Microsc.* 1984;134(2):127–136.
- 658 [26] Maisl M, Scherer T, Reiter H, Hirsekorn S. Nondestructive investigation of  
659 fibre reinforced composites by X-ray computed tomography. In: Holler P, Hauk  
660 V, Dobmann G, Ruud C, Green R, editors. Nondestructive Characterisation of  
661 Materials. Berlin: Springer-Verlag; 1988. p. 147–154.
- 662 [27] Coindreau O, Vignoles G, Cloetens P. Direct 3D microscale imaging of carbon-  
663 carbon composites with computed holotomography. *Nucl Instrum Methods*  
664 *Phys Res Sect B-Beam Interact Mater Atoms.* 2003;200:308–314.
- 665 [28] Herman GT. Image Reconstruction from Projections: The Fundamentals of  
666 Computed Tomography. New York: Academic Press; 1980.
- 667 [29] Jia X, Gopinathan N, Williams RA, Eberhardt CN, Clarke AR. X-ray  
668 microtomography facilitated modelling of microstructures. In: Proceedings 2nd  
669 World Congress on Industrial Tomography. Hannover, Germany; 2001. p. 451–  
670 460.
- 671 [30] Eberhardt CN, Clarke AR. Automated reconstruction of curvilinear fibres  
672 from 3D datasets acquired by X-ray microtomography. *J Microsc (Oxford).*  
673 2002;206(1):41–53.
- 674 [31] Buckley JD, Edie DD. Carbon-carbon materials and composites. Parkridge,  
675 NJ: William Andrew Publishing/Noyes; 1993.
- 676 [32] Christin F. Design, fabrication and application of thermostructural composites  
677 like C/C, C/SiC and SiC/SiC composites. *Adv Eng Mater.* 2002;4(12):903–912.
- 678 [33] Coindreau O. Etude 3D des preformes fibreuses: Interaction entre phenomenes

679 physico-chimiques et geometrie [PhD Thesis]. Université Bordeaux1. France;  
680 2003.

681 [34] Coindreau O, Vignoles GL. Assessment of structural and transport properties  
682 in fibrous C/C composite preforms as digitized by X-ray CMT. Part I: Image  
683 acquisition and geometrical properties. *J Mater Res.* 2005;20:2328–2339.

684 [35] Velhinho A, Sequeira PD, Martins R, Vignoles G, Fernandes FB, Botas JD,  
685 et al. X-ray tomographic imaging of Al/SiC<sub>p</sub> functionally graded composites  
686 fabricated by centrifugal casting. *Nucl Instrum Meth B.* 2003;200:295–302.

687 [36] Velhinho A, Sequeira PD, Martins R, Vignoles G, Fernandes FB, Botas JD,  
688 et al. Evaluation of Al-SiC wetting characteristics in functionally graded  
689 metal-matrix composites by synchrotron radiation microtomography. *Mater  
690 Sci Forum.* 2003;423–425:263–268.

691 [37] Bickerdike R, Brown A, Huges G, Ranson H. The deposition of pyrolytic carbon  
692 in the pores of bonded and unbonded carbon powders. In: *Proceedings of the  
693 5th AMCS Biennial Conference on Carbon; 1962.* p. 575–582.

694 [38] Besmann TM. *Processing science for chemical vapor infiltration.* Oak Ridge:  
695 Oak Ridge National Laboratory; 1990.

696 [39] Jin S, Wang X, Starr TL, Chen X. Robust numerical simulation of porosity  
697 evolution in Chemical Vapor Infiltration I: Two space dimension. *J Comp Phys.*  
698 2000;162:467–482.

699 [40] Jin S, Wang X. Robust numerical simulation of porosity evolution in Chemical  
700 Vapor Infiltration II. Two-dimensional anisotropic fronts. *J Comp Phys.*  
701 2002;179:557–577.

702 [41] Jin S, Wang X. Robust numerical simulation of porosity evolution in Chemical  
703 Vapor Infiltration III: Three space dimension. *J Comp Phys.* 2003;186:582–595.

- 704 [42] Wertheimer M. Untersuchungen zur Lehre von der Gestalt II. *Psychol Forsch.*  
705 1923;4:301–350. Translation published as Wertheimer M. *Laws of Organization*  
706 *in Perceptual Forms*. In: Ellis W, editor. *A source book of Gestalt psychology*.  
707 London: Routledge & Kegan Paul; 1938. p. 71–88.
- 708 [43] Marr D. *Vision*. San Francisco, CA: Freeman Publishers; 1982.
- 709 [44] DeValois RL, DeValois KK. *Spatial Vision*. Oxford: Oxford University Press;  
710 1990.
- 711 [45] Perona P, Malik J. Scale-space and edge detection using anisotropic diffusion.  
712 *IEEE Trans Pattern Anal Mach Intell.* 1990;12:629–639.
- 713 [46] Weickert J. *Anisotropic Diffusion in Image Processing*. Stuttgart, Germany:  
714 Teubner; 1998.
- 715 [47] Weickert J. Theoretical foundations of anisotropic diffusion in image processing.  
716 In: Kropatsch W, Klette R, Solina F, editors. *Theoretical Foundations of*  
717 *Computer Vision*. vol. 11 of *Computing Supplement*. Wien: Springer-Verlag;  
718 1996. p. 221–236.
- 719 [48] Weickert J. Coherence-enhancing diffusion filtering. *Int J Comput Vis.*  
720 1999;31(2/3):111–127.
- 721 [49] Frangakis AS, Hegerl R. Nonlinear anisotropic diffusion in three-dimensional  
722 electron microscopy. In: *Scale-Space Theories in Computer Vision*. vol. 1682 of  
723 *Lecture Notes in Computer Science*. Springer-Verlag; 1999. p. 386–397.
- 724 [50] Tschumperlé D, Deriche R. Vector-Valued Image Regularization with PDEs:  
725 A Common Framework for Different Applications. *IEEE Trans Pattern Anal*  
726 *Mach Intell.* 2005 April;27(4):1–12.
- 727 [51] Black MJ, Sapiro G, Marimont DH, Heeger D. Robust anisotropic diffusion.  
728 *IEEE Trans Image Process.* 1998;7:421–432.

- 729 [52] Nitzberg M, Shiota T. Nonlinear image filtering with edge and corner  
730 enhancement. *IEEE Trans Pattern Anal Mach Intell.* 1992;14:826–833.
- 731 [53] Catté F, Lions PL, Morel JM, Coll T. Image selective smoothing and edge  
732 detection by nonlinear diffusion. *SIAM J Numer Anal.* 1992;29:182–193.
- 733 [54] You YL, Xu W, Tannenbaum A, Kaveh M. Behavioral analysis of anisotropic  
734 diffusion in image processing. *IEEE Trans Image Process.* 1996;5:1539–1553.
- 735 [55] Kichenassamy M. The Perona-Malik paradox. *SIAM J Appl Math.*  
736 1997;57:1328–1342.
- 737 [56] Weickert J, Benhamouda B. A semidiscrete nonlinear scale-space theory and  
738 its relation to the Perona-Malik paradox. In: Solina F, Kropatsch W, Klette R,  
739 Bajcsy R, editors. *Advances in Computer Vision.* Wien: Springer-Verlag; 1997.  
740 p. 1–10.
- 741 [57] Martín-Herrero J, Alba-Castro JL. High speed machine vision: The canned tuna  
742 case. In: Billingsley J, editor. *Mechatronics and Machine Vision in Practice:*  
743 *Future Trends.* Hertfordshire, UK: Research Studies Press; 2003. p. 177–186.
- 744 [58] Clarke AR, Eberhardt CN. An automated fibre orientation measurement  
745 design. In: *Microscopy Techniques for Materials Science.* Cambridge: Woodhead  
746 Publishing; 2002. p. 202–207.
- 747 [59] Ahn SJ, Rauh W, Warnecke HJ. Least-square orthogonal distances fitting of  
748 circle, sphere, ellipse, hyperbola, and parabola. *Patt Recogn.* 2001;34:2283–  
749 2303.
- 750 [60] Brice CR, Fennema CL. Scene analysis using regions. *Artif Intell.* 1970;1(3-  
751 4):205–226.
- 752 [61] Luger GF, Stubblefield WA. *Artificial Intelligence: Structures and Strategies*  
753 *for Complex Problem Solving.* 2nd ed. New York: Chapman Hall; 1993.

- 754 [62] Rosenfeld A, Pfaltz J. Sequential operations in digital picture processing. J  
755 ACM. 1966;13:471–494.
- 756 [63] Dillencourt MB, Samet H, Tamminen M. A general approach to connected-  
757 component labeling for arbitrary image representations. J ACM. 1992;39:253–  
758 280.
- 759 [64] Tarjan RE. Efficiency of a good but not linear set union algorithm. J ACM.  
760 1975;22(2):215–225.
- 761 [65] Martín-Herrero J. Hybrid cluster identification. J Phys A: Math Gen.  
762 2004;37:9377–9386.
- 763 [66] Martín-Herrero J. Hybrid object labelling in digital images. Mach Vis Appl.  
764 2007;(in press).
- 765 [67] Weickert J, ter Haar Romeny BM, Viergever MA. Efficient and reliable  
766 schemes for nonlinear diffusion filtering. IEEE Trans Image Process. 1998  
767 March;7(3):398–410.
- 768 [68] Martín-Herrero J, Peón-Fernández J. Alternative techniques for cluster labelling  
769 on percolation theory. J Phys A: Math Gen. 2000;33:1827–1840.